

Michaël J. A. Girard¹

Department of Biomedical Engineering,
Tulane University,
6823 St. Charles Avenue,
New Orleans, LA 70118;
Ocular Biomechanics Laboratory,
Devers Eye Institute,
Legacy Health Research,
1225 NE 2nd Avenue,
Portland, OR 97232
e-mail: michael.girard@me.com

J. Crawford Downs

Ocular Biomechanics Laboratory,
Devers Eye Institute,
Legacy Health Research,
1225 NE 2nd Avenue,
Portland, OR 97232;
Department of Biomedical Engineering,
Tulane University,
6823 St. Charles Avenue,
New Orleans, LA 70118

Michael Bottlang

Biomechanics Laboratory,
Legacy Health Research,
1225 NE 2nd Avenue,
Portland, OR 97232

Claude F. Burgoyne

Optic Nerve Head Research Laboratory,
Devers Eye Institute,
Legacy Health Research,
1225 NE 2nd Avenue,
Portland, OR 97232;
Department of Biomedical Engineering,
Tulane University,
6823 St. Charles Avenue,
New Orleans, LA 70118

J.-K. Francis Suh

Moksan BioEng LLC,
605 Middle Street,
Unit No. 25,
Braintree, MA 02184;
Department of Biomedical Engineering,
Tulane University,
6823 St. Charles Avenue,
New Orleans, LA 70118

Peripapillary and Posterior Scleral Mechanics—Part II: Experimental and Inverse Finite Element Characterization

*The posterior sclera likely plays an important role in the development of glaucoma, and accurate characterization of its mechanical properties is needed to understand its impact on the more delicate optic nerve head—the primary site of damage in the disease. The posterior scleral shells from both eyes of one rhesus monkey were individually mounted on a custom-built pressurization apparatus. Intraocular pressure was incrementally increased from 5 mm Hg to 45 mm Hg, and the 3D displacements were measured using electronic speckle pattern interferometry. Finite element meshes of each posterior scleral shell were reconstructed from data generated by a 3D digitizer arm (shape) and a 20 MHz ultrasound transducer (thickness). An anisotropic hyperelastic constitutive model described in a companion paper (Girard, Downs, Burgoyne, and Suh, 2009, “Peripapillary and Posterior Scleral Mechanics—Part I: Development of an Anisotropic Hyperelastic Constitutive Model,” ASME J. Biomech. Eng., **131**, p. 051011), which includes stretch-induced stiffening and multidirectional alignment of the collagen fibers, was applied to each reconstructed mesh. Surface node displacements of each model were fitted to the experimental displacements using an inverse finite element method, which estimated a unique set of 13 model parameters. The predictions of the proposed constitutive model matched the 3D experimental displacements well. In both eyes, the tangent modulus increased dramatically with IOP, which indicates that the sclera is mechanically nonlinear. The sclera adjacent to the optic nerve head, known as the peripapillary sclera, was thickest and exhibited the lowest tangent modulus, which might have contributed to the uniform distribution of the structural stiffness for each entire scleral shell. Posterior scleral deformation following acute IOP elevations appears to be nonlinear and governed by the underlying scleral collagen microstructure as predicted by finite element modeling. The method is currently being used to characterize posterior scleral mechanics in normal (young and old), early, and moderately glaucomatous monkey eyes.*

[DOI: 10.1115/1.3113683]

Keywords: scleral mechanics, intraocular pressure, glaucoma, inverse finite element

1 Introduction

This is the second of two reports, which together propose a strategy to characterize the mechanical behavior of the posterior sclera under acute elevations of intraocular pressure (IOP). To accurately account for scleral anisotropy, we developed an anisotropic hyperelastic model in the first report [1], which incorporates multidirectional alignment of the collagen fibers at local material points. Application of this model to anatomically accurate geom-

etry of monkey posterior sclera is presented in this second report. Scleral mechanical properties are obtained by fitting the model-predicted displacements to the experimentally-measured displacements using an inverse finite element method.

In literature, estimations of scleral mechanical properties have been limited to linear and nonlinear isotropic analyses based on relatively crude optical tracking of pressurized shells [2–5] and linear and nonlinear isotropic (elastic and viscoelastic) characterizations based on uniaxial testing of scleral strips [6–17]. While these studies made important contributions to our understanding of scleral mechanics, a more comprehensive approach that characterizes the nonlinear, anisotropic nature of the sclera and its inhomogeneous fibrous ultrastructure is necessary. Because the sclera transmits IOP-related deformations to the optic nerve head

¹Corresponding author.

Manuscript received June 21, 2008; final manuscript received December 11, 2008; published online April 15, 2009. Review conducted by Ellen M. Arruda. Paper presented in part at the Association for Research in Vision and Ophthalmology Annual Meeting, Fort Lauderdale, FL, May 2007.

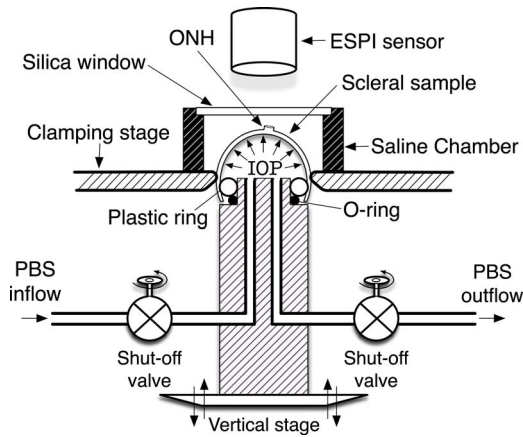


Fig. 1 Schematic showing a cross section of the custom-built pressurization apparatus. The posterior scleral shell was first mounted onto the plastic ring, and then clamped slightly above the equator by moving the vertical stage toward the clamping stage. PBS outflow was interrupted after PBS filled the posterior shell cavity and IOP reached 5 mm Hg. The scleral surface was imaged as IOP was increased from 5 mm Hg to 45 mm Hg.

(ONH) and is altered in early experimental glaucoma [10], knowledge of scleral mechanics is essential to evaluate how the tissues of the ONH respond to IOP. This information is vital in developing a clear understanding of the role of IOP in the development and progression of glaucoma—an optic neuropathy caused by retinal ganglion cell axon damage at the ONH [18,19].

2 Materials and Methods

2.1 Experimental Setup and Testing Protocol. Specimen preparation. One male rhesus monkey (2.1 years old) without any apparent optic abnormality was anesthetized with an intramuscular injection of ketamine/xylazine and sacrificed with an intravenous injection of sodium pentobarbital. After enucleation, both eyes were carefully cleaned of extra-orbital tissues, and the posterior sclera was separated from the anterior chamber approximately 3 mm anterior to the equator. The retina and choroid were carefully dissected away from the scleral shell except for a 7-mm-diameter patch centered on the ONH, which was left intact to prevent fluid leakage from the ONH during pressurization. All ocular tissues were kept moist with phosphate buffered saline (PBS) throughout the specimen preparation.

Measurement of scleral surface displacements. The posterior scleral shells from both eyes were individually mounted on a custom-built pressurization apparatus (Fig. 1) and internally pressurized using a column of PBS at 22°C. IOP was controlled at a resolution of 0.01 mm Hg by altering the PBS column height with a motor-driven stage (Bislide, Velmex, Bloomfield, NY) and monitored by a digital pressure gauge (X2Pi, Crystal Engineering, San Luis Obispo, CA). To enhance its optical contrast, each shell surface was blotted dry and treated with white titanium powder (ProCAD Contrast Medium, Ivoclar, Schaan, Lichtenstein) diluted in a 70% ethanol solution. A custom-built chamber was then mounted above the shell and filled with 50 ml of PBS to maintain specimen hydration. The chamber was fabricated with a silica window coated with an antireflective film to optimize displacement measurements of the shell surface with an electronic speckle pattern interferometry (ESPI) sensor (Q100, Ettemeyer AG, Germany) [20,21].

Each shell was subjected to IOP preconditioning, consisting of 20 IOP cycles from 5 mm Hg to 15 mm Hg at a rate of 5 mm Hg/s, and then allowed to recover for 360 s. IOP was then increased from 5 mm Hg to 10 mm Hg in steps of 0.2 mm Hg,

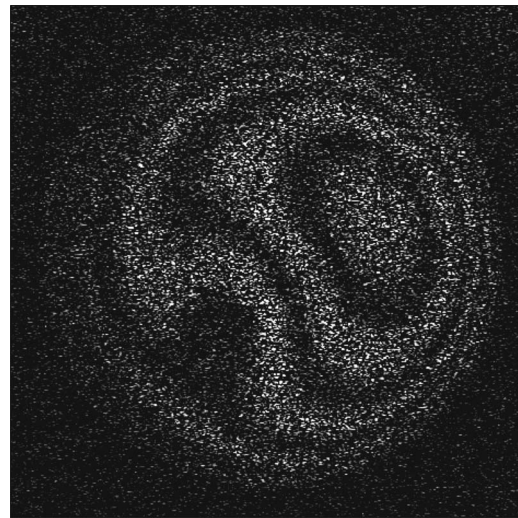


Fig. 2 Example of raw speckle fringes (one of four illumination directions from the ESPI sensor) on a rubber balloon for an IOP increase from 10 mm Hg to 10.2 mm Hg. The distance between the fringes is proportional to the 3D displacement of the balloon surface.

from 10 mm Hg to 30 mm Hg in steps of 0.4 mm Hg, and from 30 mm Hg to 45 mm Hg in steps of 0.6 mm Hg. Because sclera stiffens with increasing IOP, the IOP step magnitude was increased to keep the resultant displacements within the measurable range of the ESPI sensor. For each IOP step, the ESPI sensor captured laser speckle images over a 35×25 mm² area at an equilibrium state. An example of such image is depicted in Fig. 2. Each displacement component (x, y, z) was then computed using speckle image algorithms for each IOP step at a resolution of 0.1 μm and reported in a 256×256 matrix format that covered the entire measuring area. Finally, each component was summed over the following IOP intervals: 5–7 mm Hg, 5–10 mm Hg, 5–20 mm Hg, 5–30 mm Hg, and 5–45 mm Hg. These IOP intervals correspond to the physiologic range and were chosen because they are directly comparable to the in vivo, image-based ONH compliance testing and perfusion fixation protocols used in our other monkey studies [22,23].

Measurement of scleral surface geometry. The following experiment consisted in obtaining the surface geometry of the shell in its reference state (IOP of 5 mm Hg). Once the acquisition of the ESPI images was completed, IOP was lowered from 45 mm Hg to 5 mm Hg, and the shell was allowed to equilibrate. The outer surface geometry of the shell was then manually digitized using a 3D digitizer arm (MicroScribe G2X, Immersion, San Jose, CA). For each shell, the Cartesian coordinates of 1000 spatial points were recorded to cover the entire scleral surface. The scleral canal and the clamping area were also digitized to provide boundaries for the scleral specimen.

Measurement of scleral thickness. Scleral thickness was measured using a 20 MHz ultrasound transducer (PacScan 300P, Sonomed, Inc., Lake Success, NY), combined with a 75 MHz pulser-receiver (5073PR, Olympus NDT, Inc., Waltham, MA) and a 200 MHz digital oscilloscope (TDS2022, Tektronix, Beaverton, OR). This measurement system was able to acquire a minimum thickness of 100 μm at a resolution of 1 μm .

Prior to thickness measurements, 20 spatial points were marked on the scleral surface with a fine tip marker (Fig. 3(a)) and their Cartesian coordinates were recorded with the 3D digitizer arm. To enhance acoustic energy reflection at the inner surface of the sclera, the PBS inside the scleral shell was replaced with moist air controlled by a pressure regulator (Model 81, Fairchild, Winston-Salem, NC) and the shell was pressurized to 5 mm Hg. The ul-

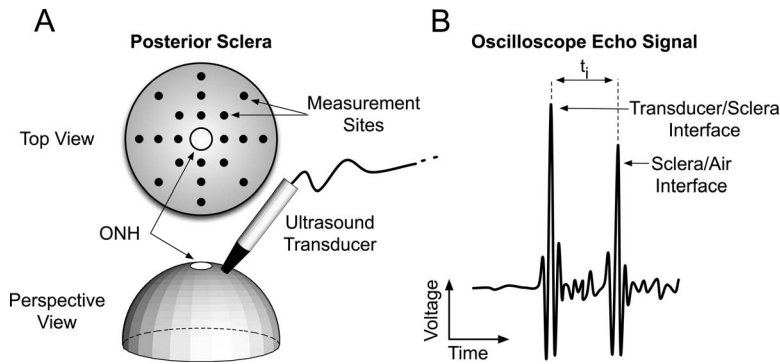


Fig. 3 (a) Location of the 20 thickness measurement sites, shown as black dots on the outer surface of the posterior sclera. For each location, the 20 MHz ultrasound transducer was positioned perpendicular to the scleral surface, and the corresponding voltage echo signal was recorded in order to extract scleral thickness. (b) An example of a voltage echo signal obtained from the oscilloscope for one measurement site. $\frac{1}{2}t_i$ is the time taken by an acoustic wave to travel from the transducer/sclera interface to the sclera/air interface.

trasound transducer was then positioned perpendicular to each of the 20 predetermined points, and voltage echo signals were collected on the oscilloscope (Fig. 3(b)). Scleral thickness, d_i , was calculated at each point according to the following formula:

$$d_i = \frac{1}{2}v_{\text{sclera}} \cdot t_i, \quad i \in [1, 20] \quad (1)$$

where v_{sclera} is the speed of sound in the sclera, which was set to 1597 m/s [24], and t_i is the echo time, which was determined from the oscilloscope signal (Fig. 3(b)).

2.2 Finite Element (FE) Modeling. FE mesh. The surface geometry and thickness data were combined to generate a finite element (FE) mesh of the specimen using custom-written MATLAB subroutines (MATLAB, The Mathworks, Natick, MA). Briefly, the digitized boundaries of the clamp and the scleral canal were fitted to a circle and an ellipse, respectively, using a least-square algorithm. The point cloud of the scleral surface was then smoothed using the thin-plate spline method, and thickness data were interpolated over the entire scleral surface field. These data were combined to generate a FE mesh with eight-noded hexahedral elements using grid projection methods. The FE mesh was divided into nine subregions, where regions 1–4 contain the peripheral sclera, regions 5–8 contain the peripapillary sclera, and region 9 represents the ONH (Fig. 4(a)). A convergence test was performed to assess the numerical accuracy of the FE approximation by increasing the number of nodes. Adequate numerical accuracy was achieved with 5091 nodes and 3328 elements.

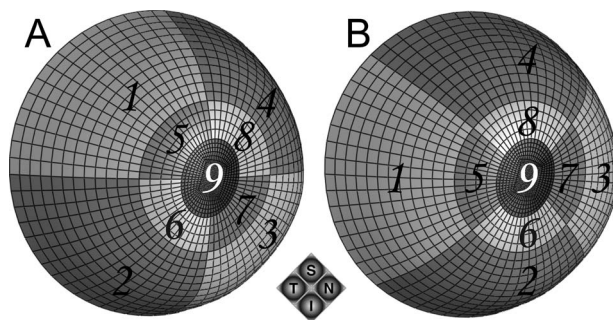


Fig. 4 (a) FE model of the monkey posterior scleral shell of a left eye showing one regionalization pattern. Regions 1–4 are the peripheral sclera, regions 5–8 are the peripapillary sclera, and region 9 is the ONH. (b) Same FE mesh as (a), but with a different regionalization pattern. S, superior; N, nasal; I, inferior; and T, temporal.

Model assumptions. In incorporating the fiber-reinforced constitutive theory for ocular soft tissues developed in Part I [1] into FE models of the posterior scleral shell, several assumptions were made. (1) The mechanical properties of the collagen fibers are generic and uniform throughout the scleral tissue. (2) The mechanical properties of the ground substance matrix are generic and uniform throughout the scleral tissue. (3) Regional variation in the mechanical response of the scleral shell is principally governed by inhomogeneity of the collagen fiber ultrastructure, which can be quantitatively described using the preferred fiber orientation and the fiber concentration factor. (4) The collagen fiber alignment in the peripapillary sclera differs from that in the peripheral sclera. Based on these assumptions, three model parameters (c_1 , first Mooney–Rivlin coefficient; c_3 , exponential fiber stress coefficient; and c_4 , fiber uncrimping coefficient) were uniformly attributed to the entire posterior sclera. Two fiber concentration factors, k_1 and k_2 , were attributed to the peripheral sclera (regions 1–4) and peripapillary sclera (regions 5–8), respectively. Individual preferred fiber orientations, $\theta_{p1} - \theta_{p8}$, were attributed to each region (Fig. 5).

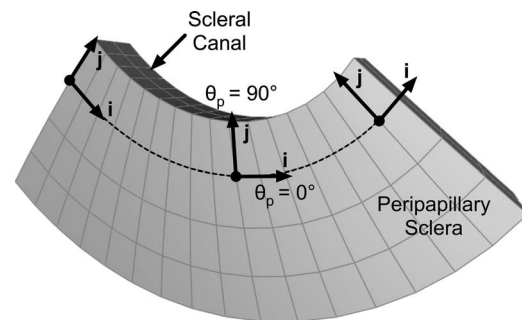


Fig. 5 One subregion of the peripapillary sclera of a left monkey eye, showing how collagen fiber alignment was defined. For each hexahedral element, the local unit vector i was constructed with element edge information. The local unit vector j was constructed as being perpendicular to the unit vector i and tangent to the scleral surface. Unit vectors i and j define the plane in which the collagen fibers lie. Although each element of this subregion shares the same preferred fiber orientation θ_p , the unit vector associated with θ_p will be different for each element in the global coordinate system. For example, if the preferred fiber orientation is equal to zero for this subregion ($\theta_p = 0$ deg), collagen fibers will be oriented along the unit vector i (for $k \neq 0$), corresponding to a circumferential organization.

As a consequence, the FE model contained a total number of 13 model parameters to be determined. In addition, the bulk modulus of the sclera K was fixed at 1 GPa to assure incompressibility, and the ONH was modeled as an incompressible linear isotropic material with an elastic modulus (E_{ONH}) of 1 MPa.

Boundary and loading conditions. For each FE model, IOP was numerically applied to the interior surface of the shell as a uniform pressure load. Nodes belonging to both the peripheral sclera and the clamping boundary were constrained in all three directions in order to maintain consistency with restraints imposed by the clamp in the experimental protocol. For simplicity, the reference geometry generated at 5 mm Hg was assumed to be stress-free.

2.3 Extraction of Scleral Model Parameters: Inverse FE Method. Scleral model parameters were extracted using an inverse FE method, in which an optimization algorithm, i.e., differential evolution [25], was coupled with the FE method. The differential evolution algorithm sought to determine the set of 13 model parameters that yielded the closest match between the FE-simulated and the experimentally-measured displacements. Numerically, the surface node displacements of the FE model were fitted to their colocalized experimental values simultaneously at five IOP levels (7 mm Hg, 10 mm Hg, 20 mm Hg, 30 mm Hg, and 45 mm Hg) by minimizing the following cost function ε :

$$\varepsilon = \frac{1}{N \cdot P} \sum_{n=1}^N \sqrt{\sum_{p=1}^P [(x_{n,p}^e - x_{n,p}^m)^2 + (y_{n,p}^e - y_{n,p}^m)^2 + (z_{n,p}^e - z_{n,p}^m)^2]} \quad (2)$$

Here, $(x_{n,p}^e, y_{n,p}^e, z_{n,p}^e)$ and $(x_{n,p}^m, y_{n,p}^m, z_{n,p}^m)$ are the three components of the experimental (e) and model (m) displacements, respectively, at surface node n and an IOP level of p , N is the total number of surface nodes, and P is the total number of IOP levels.

Our preliminary study with the differential evolution algorithm showed that a weighting factor F of 0.5, a crossover constant CR of 0.9, and a number of trial vectors (i.e., sets of the 13 model parameters) NP of 50 were well suited for our inverse FE problem. These parameters were chosen using the knowledge we developed for previous inverse problems we have solved in our laboratories [12,26]. The reader is referred to the work of Price et al. for a better understanding of the differential evolution algorithm parameters [25]. The following initial ranges were used with the differential evolution algorithm for the considered model parameters: $0 \leq c_1 \leq 1000$, $0 \leq c_3 \leq 100$, $0 \leq c_4 \leq 1000$, $0 \leq (k_1, k_2) \leq 20$, and $0 \leq (\theta_{p1}, \dots, \theta_{p8}) \leq 180$. It should be noted that the differential evolution algorithm has strong advantages over other global optimization algorithms because it is easy to implement, does not require a single initial guess, and allows the parameters to evolve beyond their initial ranges [25]. This last point is often important at the initial stages of solving a new global optimization problem. However, for the preferred fiber orientations, $\theta_{p1} - \theta_{p8}$, we implemented a custom periodicity constraint so that they could only evolve within the half circle defined by 0 deg and 180 deg.

The inverse FE simulation consisted of 450 iterations of the differential evolution algorithm. Each iteration included 50 FE runs yielding a total of 22,500 ($=450 \times 50$) FE runs. The simulation was executed on an ION computational server, with 32 Gbytes of RAM and four 64 bit Itanium2 processors (Intel, Santa Clara, CA), using a parallel queuing system written in the script language PERL (The Perl Foundation). One inverse FE simulation typically took 2 days to obtain full convergence.

2.4 Sensitivity Analyses of the Inverse FE Method. Solution uniqueness. To examine whether the inverse FE simulation yields a unique solution, pseudo-experimental displacements were generated by the FE model using several predetermined sets of arbitrary model parameters. Inverse FE simulations were then performed to test whether these model parameters could be retrieved.

Effects of regionalization pattern. Two different regionalization patterns (Fig. 4) were defined for both eyes to further assess solution uniqueness of the model parameters: c_1 , c_3 , c_4 , k_1 , and k_2 . Because c_1 , c_3 , and c_4 were uniformly attributed to the entire posterior sclera, k_1 to the peripheral sclera, and k_2 to the peripapillary sclera, inverse FE simulations are expected to yield comparable values of these model parameters for both regionalization patterns.

Effects of ONH elastic modulus. The ONH, which contains the lamina cribrosa and the retinal ganglion cell axons, was considered as a linear isotropic material. To quantify the effects of ONH mechanics on scleral mechanics, inverse FE simulations were performed with ONH elastic moduli E_{ONH} of 0.1 MPa, 1 MPa, and 5 MPa [27] for both eyes.

Effects of scleral bulk modulus. To study the stability of the incompressibility constraint, inverse FE simulations were performed with scleral bulk moduli K of 1.0 GPa and 0.1 GPa for both eyes.

2.5 Scleral Tangent Modulus. The model parameters c_3 and c_4 as obtained from the inverse FE simulations describe the non-linearity of the sclera, but do not provide a direct measure of scleral stiffness at each IOP elevations. To provide a relationship between scleral stiffness and IOP, we have isolated components of the spatial elasticity tensor \mathbf{c} . In the FE implementation of the constitutive theory, \mathbf{c} was expressed in a fixed global coordinate system [1] and can now be transformed to the local fiber coordinate system as follows:

$$c'_{ijpn} = \mathbf{a}_{iq} \mathbf{a}_{js} \mathbf{a}_{pk} \mathbf{a}_{nm} c_{qskm} \quad (3)$$

where \mathbf{c}' is the spatial elasticity tensor in the local fiber coordinate system and \mathbf{a} is the transformation matrix. Accordingly, c'_{1111} and c'_{2222} were defined as the tangent moduli along and perpendicular to the preferred fiber orientation, respectively. Both quantities are inhomogeneous, and their directions lie in the plane tangent to the shell surface.

2.6 Scleral Structural Stiffness. Clinical discussions of the corneo-scleral shell often confuse the effects of its mechanical properties and geometry on its overall mechanical behavior. We therefore attempted to take regional variations in scleral thickness into account by empirically defining the structural stiffnesses S_1 and S_2 at any point in the scleral shell as

$$\begin{aligned} S_1 &= T \cdot c'_{1111} \\ S_2 &= T \cdot c'_{2222} \end{aligned} \quad (4)$$

where T is the local scleral thickness and S_1 and S_2 are the structural stiffnesses along and perpendicular to the preferred fiber orientation, respectively.

3 Results

Sensitivity analyses. In all studies of solution uniqueness, the inverse FE simulations predicted values for all 13 model parameters perfectly with a cost function value of zero. Based on these data, the inverse FE method yields unique solutions. Results for all other sensitivity analyses are listed in Table 1. Overall, changing the scleral bulk modulus K from 0.1 GPa to 1 GPa had very little impact on all model parameters. Changing the ONH elastic modulus from 0.1 MPa to 5 MPa had some impact and resulted in an increase in c_3 and k_2 and a decrease in c_1 , c_4 , and k_1 consistently for both eyes. Changing the configuration scheme had its largest influence on c_3 and k_1 in the left eye and on k_1 in the right eye. Overall, the mean tangent moduli (c'_{1111} and c'_{2222}) were much less sensitive; C'_{1111} (mean) varied between 8.4 MPa and 10.7 MPa in the left eye and between 9.0 and 10.0 in the right eye. These results suggest that moderate variations in c_1 , c_3 , c_4 , k_1 , and k_2 induce small variations in tangent moduli. As a result, we used

Table 1 Model parameters and mean tangent moduli for the whole sclera (IOP=30 mm Hg) obtained from inverse FE simulations for both eyes. The regionalization pattern (A: Fig. 4(a); B: Fig. 4(b)), the ONH elastic modulus, and the scleral bulk modulus were varied as presented in gray. The data in bold, where $E_{\text{ONH}}=1$ MPa and $K=1$ GPa, were selected as the default case for Figs. 6 and 7 and Table 2. c'_{1111} and c'_{2222} are the tangent moduli along and perpendicular to the preferred fiber orientation, respectively.

Input	Regionalization pattern	A	A	B	A	A
	E_{ONH} (MPa)	0.1	1	1	1	5
	K (GPa)	1	1	1	0.1	1
Left eye output	c_1 (kPa)	249	193	178	197	123
	c_3 (kPa)	5.0	6.8	9.8	6.2	12.0
	c_4 (-)	631	563	621	602	455
	k_1 (-)	2.63	2.15	1.41	2.25	1.55
	k_2 (-)	2.33	2.51	2.32	2.65	3.15
	ε (μm)	2.44	2.34	2.46	2.34	2.29
	c'_{1111} (MPa) 30 mm Hg	10.7	9.7	9.5	10.4	8.4
	c'_{2222} (MPa) 30 mm Hg	3.9	3.9	5.6	4.0	3.7
Right eye output	c_1 (kPa)	156	99	86	100	65
	c_3 (kPa)	14.4	16.5	16.3	15.6	23.4
	c_4 (-)	487	475	457	505	409
	k_1 (-)	1.47	1.33	1.00	1.40	1.26
	k_2 (-)	3.51	4.40	4.12	4.57	4.99
	ε (μm)	2.39	2.35	2.51	2.34	2.42
	c'_{1111} (MPa) 30 mm Hg	9.4	9.5	9.0	10.0	9.0
	c'_{2222} (MPa) 30 mm Hg	5.7	6.3	6.3	6.6	6.0

the regionalization pattern in Fig. 4(a), $K=1$ GPa and $E_{\text{ONH}}=1$ MPa for all subsequent analyses.

Experimental and modeling results. Figure 6 depicts both experimentally-measured and model-predicted displacements in left and right eyes as IOP increased from 5 mm Hg to 10 mm Hg, from 10 mm Hg to 30 mm Hg, and from 30 mm Hg to 45 mm Hg, respectively. The displacements predicted by the model captured the complex displacement patterns of the experimental data well, and the maximum cost function value was 2.51 μm for all the cases studied. Displacement magnitude in all directions was lowest as IOP increased from 30 mm Hg to 45 mm Hg. This implies that sclera is relatively compliant when IOP is low (5–10 mm Hg), but dramatically stiffens as IOP increases beyond 30 mm Hg.

Scleral thickness for both eyes, which was acquired at 5 mm Hg and interpolated over the entire scleral region, is presented in Fig. 7. In all eyes, the peripapillary sclera was much thicker than the peripheral sclera. Figure 7 also includes additional results at an IOP of 30 mm Hg obtained from the inverse FE simulations. Note that there is an inverse relationship, but not strong, between scleral tangent modulus and scleral thickness, as depicted in Fig. 8. The structural stiffness, the local product of the tangent modulus and thickness, slightly captured this trend (Fig. 7) but was found to be on average higher in the peripapillary sclera (Table 2). From Fig. 7, the collagen fibers are generally circumferentially oriented around the ONH in three of the four subregions of the peripapillary sclera. Notice that the fibers from the peripapillary sclera were associated with a higher fiber concentration factor ($k_2 > k_1$ in Table 1), meaning a stronger anisotropy near the ONH.

The most critical output quantities (c'_{1111} , c'_{2222} , S_1 , S_2 , 1st principal strain, and 1st principal stress) for $K=1$ GPa and $E_{\text{ONH}}=1$ MPa are summarized in Table 2 for the 5th, 50th (median), and 95th percentiles of their distributions for both the peripheral and peripapillary sclera at IOPs of 10, 30 and 45 mm Hg. As seen in Table 2, the mean tangent moduli, c'_{1111} and c'_{2222} , are three to six times higher at 45 mm Hg than at 10 mm Hg in both eyes. In addition, the mean first principal strain is a nonlinear function of

IOP. Finally, the mean first principal strain is higher in the peripapillary sclera, whereas the mean first principal stress is higher in the peripheral sclera.

4 Discussion

In this report, we introduce an experimental method to measure the 3D displacements of monkey posterior sclera exposed to acute elevations of IOP from 5 mm Hg to 45 mm Hg and use the anisotropic hyperelastic model developed in Part I [1] along with an inverse FE method to extract scleral mechanical properties. Our findings demonstrate that our constitutive model can accurately predict the experimental 3D displacements of the posterior scleral shell and that the proposed inverse FE method can estimate a unique set of 13 model parameters. We have thus captured the inhomogeneous, anisotropic, and nonlinear behavior of the posterior sclera when exposed to acute elevations of IOP.

This study used a pressurization test to measure scleral deformations under pressure load. Unlike traditional biaxial patch tests, the pressurization methodology allowed us to estimate mechanical properties for the entire posterior scleral shell in its physiologic configuration. In addition, the IOP range commonly experienced by normal and glaucomatous eyes was covered in one test setup. Biaxial testing of an entire posterior scleral shell would require tests of scleral patches excised from many adjacent points, each of which would have to be flattened prior to loading.

The results from our sensitivity study showed that the scleral bulk modulus, chosen large to ensure incompressibility, can vary between 0.1 GPa and 1 GPa without affecting the overall mechanical behavior of the posterior sclera. Note that incompressibility in scleral tissue has been confirmed experimentally by Battaglioli and Kamm [28]. The other sensitivity analyses suggest that moderate variations in some of our model parameters result in slight variations in tangent moduli. Therefore, according to Table 1, we are confident to suggest that the ONH elastic modulus in the 0.1–5 MPa range will minimally affect the mechanical behavior of the posterior sclera and that a change in regionalization scheme will lead to similar model parameter estimates, thus reinforcing our preliminary study on solution uniqueness. Because the tangent

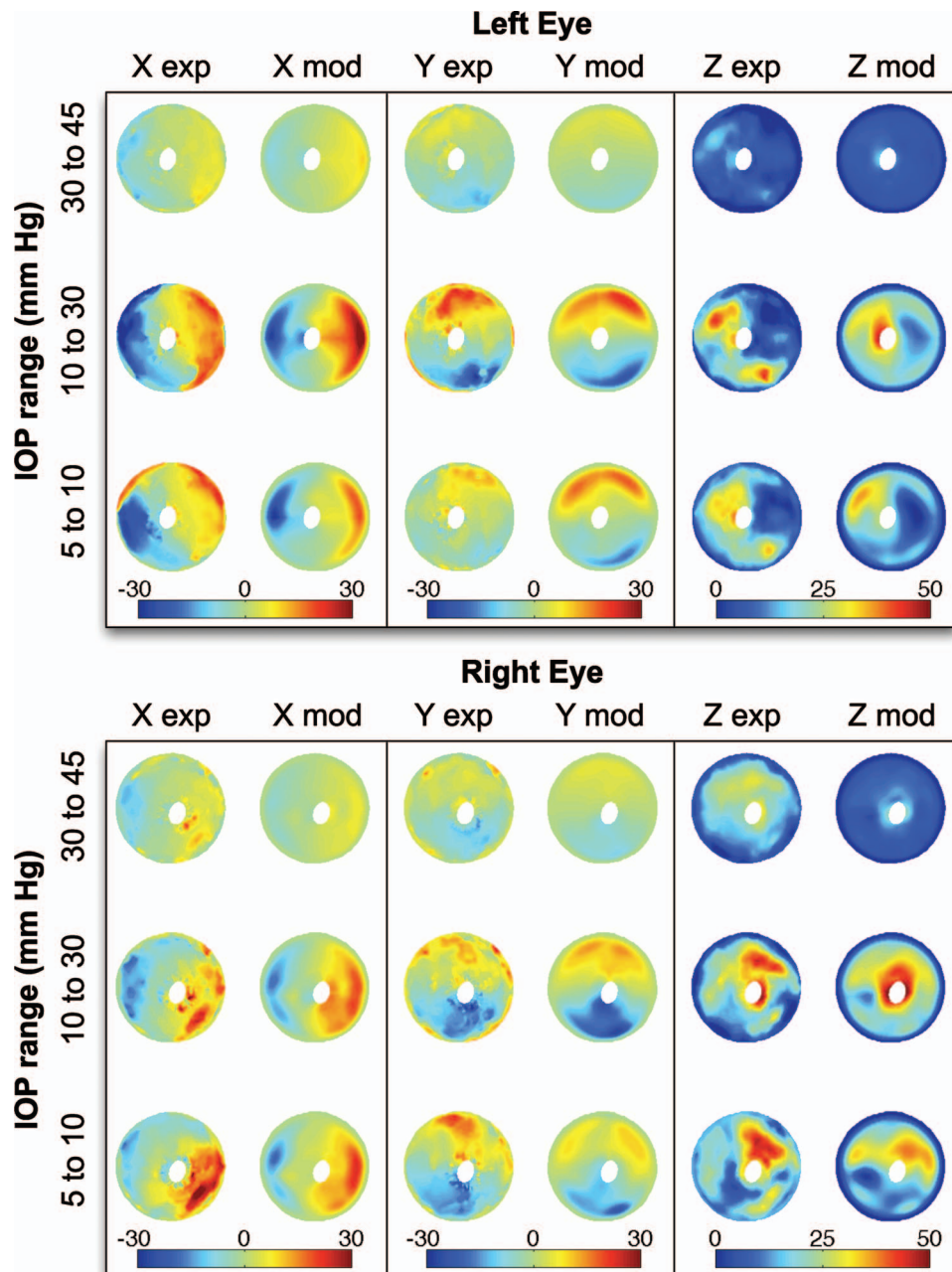


Fig. 6 Comparison of experimentally-measured (exp) and model-predicted (mod) displacements (in micrometers) for both eyes for three IOP ranges (5–10 mm Hg, 10–30 mm Hg, and 30–45 mm Hg). Model displacements were simultaneously fitted to the experimental data obtained at 7 mm Hg, 10 mm Hg, 20 mm Hg, 30 mm Hg, and 45 mm Hg. Both experimental and model displacements are small for the 30–45 mm Hg IOP range, demonstrating a high degree of nonlinearity.

moduli are less prone to variations and easier to interpret as they are functions of IOP, we are currently developing a method to compare tangent modulus distributions so as to estimate changes in scleral stiffness between normal (young and old) and glaucomatous monkey eyes, which will be the topic of further reports.

The models predicted that, in the posterior sclera of monkey eyes, the collagen fibers were generally circumferentially oriented around the ONH in three of the four subregions of the peripapillary sclera, which is consistent with previous histologic results [29]. Furthermore, collagen fibers tended to be more highly concentrated along their preferred orientations in the peripapillary sclera, as shown by the higher fiber concentration factor k_2 . This

finding is also consistent with the literature that provides qualitative descriptions of the collagen fiber microstructure in the peripapillary and peripheral sclera. In the region immediately adjacent to the ONH, elastin and collagen fibers are highly aligned and organized into a circumferential ring around the scleral canal [29], whereas the collagen fibers in the peripheral sclera are irregularly arranged to form interwoven lamellae [30–32]. As seen in our first report [1], a high fiber concentration factor associated with a circumferential fiber organization will limit scleral canal expansion, and this may help the peripapillary sclera to protect the ONH although it should be noted that small scleral canal expansion is usually associated with large posterior lamellar deformation.

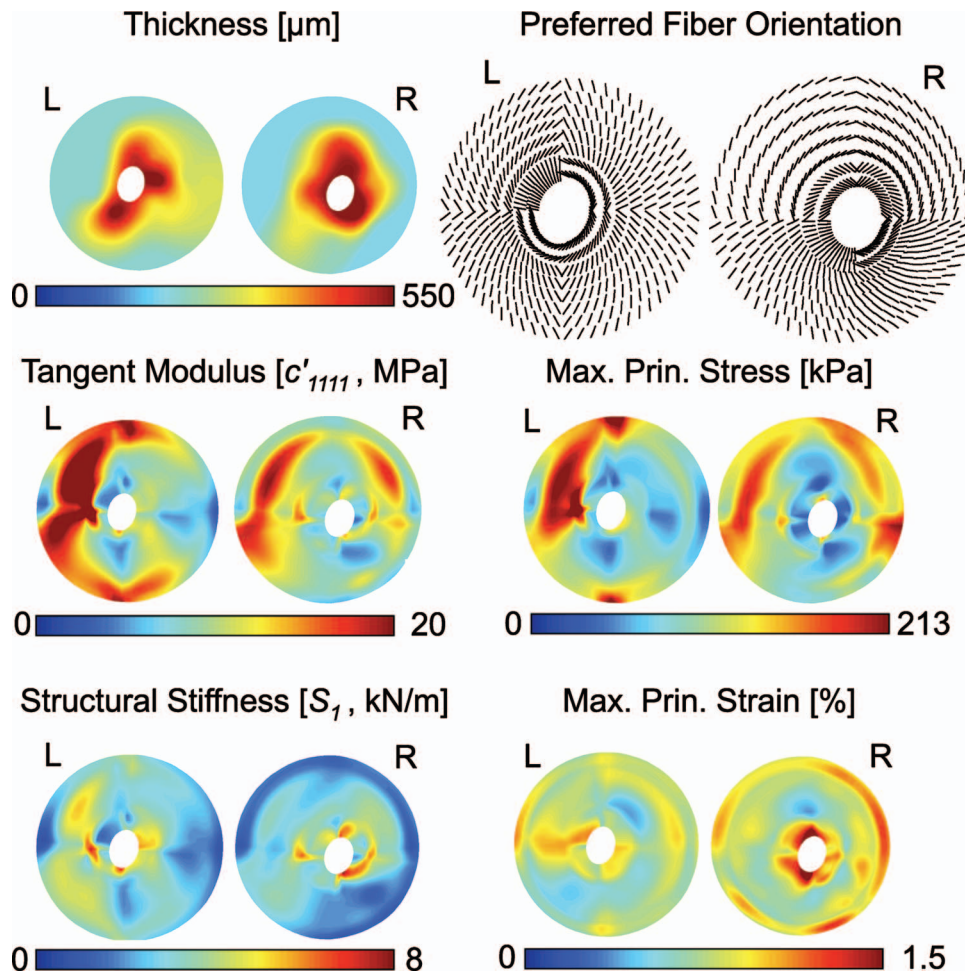


Fig. 7 The main modeling results are shown as color maps for both eyes at an IOP of 30 mm Hg. Scleral thickness maps were derived from experimental ultrasound measurements at 5 mm Hg and show that the peripapillary sclera is much thicker than the peripheral sclera. An inverse relationship between scleral thickness and scleral tangent modulus c'_{1111} was observed, indicating that thinner sclera is likely to be associated with a higher tangent modulus. The structural stiffness along the preferred fiber orientation, S_1 , helps visualize this inverse relationship. Finally, maximum principal strain was concentrated around the scleral canal.

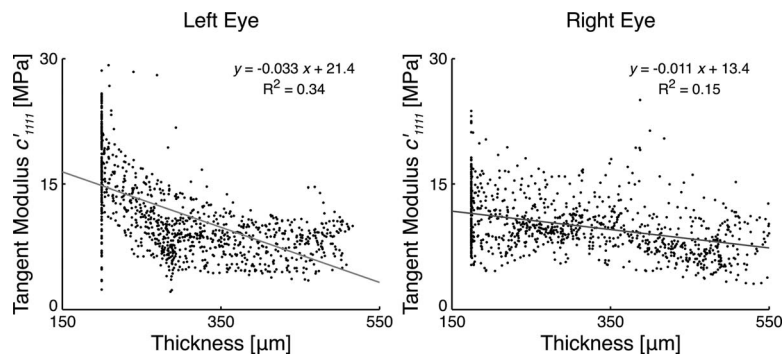


Fig. 8 Tangent modulus c'_{1111} versus scleral thickness for both eyes at an IOP of 30 mm Hg, which illustrates the concept of inverse relationship between two quantities. A thin sclera (the peripheral sclera) has a tendency to be associated with larger c'_{1111} and a thick sclera (the peripapillary sclera) with smaller c'_{1111} . Notice small R^2 values obtained from linear regression analyses, possibly due to the scatteredness of the data points.

Table 2 5th, 50th (median), and 95th percentiles of the tangent moduli, structural stiffnesses, and first principal strain and first principal stress distributions for IOP=10 mm Hg, 30 mm Hg, and 45 mm Hg and for both the peripheral and peripapillary sclera of both eyes. S_1 and S_2 are the structural stiffnesses along and perpendicular to the preferred fiber orientation, respectively.

IOP (mm Hg)			5th percentile			50th percentile			95th percentile			
			10	30	45	10	30	45	10	30	45	
Left eye	Peripapillary sclera	c'_{1111} (MPa)	2.1	4.5	6.6	2.6	8.2	13.0	3.4	13.8	22.5	
		c'_{2222} (MPa)	0.9	2.1	3.2	1.0	3.8	6.7	1.2	7.1	13.5	
		S_1 (kN/m)	0.8	1.7	2.4	1.1	3.4	5.3	1.5	5.8	9.7	
		S_2 (kN/m)	0.3	0.9	1.3	0.4	1.6	2.9	0.5	2.8	5.2	
		First prin. strain (%)	0.18	0.57	0.70	0.31	0.86	1.01	0.44	1.07	1.25	
		First prin. stress (kPa)	5.1	27.3	44.5	8.4	51.9	87.2	13.4	90.9	162	
		Peripheral sclera	c'_{1111} (MPa)	1.9	3.4	4.8	3.1	10.0	15.8	5.0	22.3	36.3
	c'_{2222} (MPa)		0.9	1.5	2.0	1.2	3.9	6.3	1.7	8.0	13.9	
	S_1 (kN/m)		0.5	0.8	1.2	0.9	2.8	4.5	1.2	4.9	7.8	
	S_2 (kN/m)		0.2	0.4	0.5	0.3	1.1	1.7	0.4	1.9	3.3	
	First prin. strain (%)		0.17	0.49	0.61	0.30	0.75	0.88	0.47	1.00	1.20	
	First prin. stress (kPa)		3.8	13.4	21.7	11.3	58.9	95.7	25.8	140	226	
	Right eye	Peripapillary sclera	c'_{1111} (MPa)	3.5	4.7	6.0	4.1	7.9	11.0	4.8	12.7	19.5
			c'_{2222} (MPa)	1.0	1.3	1.8	1.1	2.1	3.2	1.3	3.7	7.5
S_1 (kN/m)			1.5	2.2	2.7	1.9	3.6	5.0	2.5	6.3	9.8	
S_2 (kN/m)			0.4	0.6	0.8	0.5	1.0	1.4	0.7	1.9	3.7	
First prin. strain (%)			0.25	0.79	0.97	0.35	1.06	1.28	0.54	1.57	1.84	
First prin. stress (kPa)			3.6	16.1	26.4	7.1	36.1	59.5	11.3	73.7	136	
Peripheral sclera			c'_{1111} (MPa)	2.6	4.6	6.4	3.7	9.9	14.8	5.2	17.2	26.3
		c'_{2222} (MPa)	1.3	3.0	4.3	1.8	7.0	11.1	2.7	12.9	20.7	
		S_1 (kN/m)	0.5	1.0	1.4	0.9	2.5	3.8	1.5	4.3	6.5	
		S_2 (kN/m)	0.3	0.6	0.8	0.5	1.8	2.8	0.7	2.8	4.5	
		First prin. strain (%)	0.21	0.55	0.66	0.35	0.79	0.94	0.51	1.19	1.58	
		First prin. stress (kPa)	5.4	26.8	43.4	13.4	68.1	109	26.8	132	211	

In the experimental pressure tests, we observed a high degree of nonlinearity that was manifested by much smaller incremental displacements when IOP was elevated above 30 mm Hg, which was also measured in porcine sclera in our previous study [33]. This nonlinearity was additionally observed in the tangent moduli and structural stiffnesses as they exponentially increased with IOP from 5 mm Hg to 45 mm Hg.

Physiologically, the sclera is a load bearing structure to resist IOP and yet the eye may need to maintain its shape to preserve focused vision. Thus, it seems reasonable to assume that scleral thickness and tangent modulus should balance each other to ensure that the eye expands in a somewhat uniform manner with increasing IOP. In this study, we found an inverse relationship, but not strong, between scleral thickness and tangent modulus (Fig. 8). We have also defined an empirical measure, namely, the structural stiffness, to capture this trend (Fig. 7). It should be noted that in the case of an idealized scleral shell geometry of spherical shape, constant thickness, and constant elastic modulus (using linear elastic theory), our definition of structural stiffness would be uniform for the entire scleral shell (i.e., constant elastic modulus \times constant thickness). This ideal case would ensure homogeneous deformations within the peripheral sclera but not within the peripapillary sclera because of the discontinuity within the scleral shell due to the presence of the scleral canal. In fact, in our case, the structural stiffness was on average higher in the peripapillary sclera (Table 1), which might be a protective mechanism to minimize the deformations in the vicinity of the ONH. However, further study will be necessary to understand the relationship between the ultrastructural characteristics and the overall deformational behavior of the posterior sclera.

Several limitations should be taken into consideration when viewing this work. First, we were unable to measure the 3D deformations of each scleral shell during preconditioning because the ESPI sensor requires about 4 s to acquire raw deformation

data. Therefore, we were unable to carefully characterize the deformational behavior of the sclera during preconditioning, which could have caused permanent deformations in the tissue. However, because the normal IOP range in rhesus monkeys has been reported to be 14.9 ± 2.1 mm Hg [34], it is unlikely that preconditioning the tissues up to an IOP of 15 mm Hg would have induced any damage or permanent change in the tissue.

Second, we have assumed that the collagen fibers were the sole contributors to the nonlinear relationship between IOP and scleral deformations and that the relative contributions of ground substance and collagen fibers to scleral mechanical properties were uniform throughout the scleral shell. These assumptions are well established when characterizing the mechanical behavior of collagenous soft tissues [35], but more work may be needed to characterize the influence of other constituents such as elastin and the effects of regional changes in collagen fiber diameter.

Third, the mechanical deformations for IOPs below 5 mm Hg have not been accounted for in this study because the scleral shells did not acquire their pressurized geometry until approximately 4 mm Hg of IOP was applied. Physiologic IOP for normal monkey eyes is generally above 5 mm Hg, but including information below 5 mm Hg could improve the model's predictions. In the future, one might attempt to resolve this computationally using the inverse elastostatic method [36,37] to mathematically recover the initial stress-free configuration of an elastic body. However, this method is only valid on the premise that residual stresses are insignificant, which is not known for monkey posterior sclera.

Fourth, the boundary of the ONH was represented in the model using an ellipse fitted to the outer aspect of the dural sheath insertion and was therefore larger than one would expect (~ 2 mm along the major axis in our model, compared with ~ 1.5 mm for an anatomic ONH). In addition, the ONH was modeled as a linear

elastic plug of the same curvature and thickness of the surrounding sclera, but with its own modulus. Our sensitivity studies showed that the overall model behavior of the posterior sclera was not sensitive to the mechanical properties of the ONH, so these model assumptions have little impact on the reported results. On the contrary, the mechanical behavior of the ONH has been reported to be very sensitive to the mechanical properties of the posterior sclera [38]. This is consistent with the study conducted in Part I [1] showing that the distribution of the scleral collagen fibers had large effects on scleral canal expansion and laminar posterior deformation. However, in order to fully understand the interaction between the sclera and the ONH, more accurate data including the geometry of the scleral canal and the ONH as well as the mechanical properties of the ONH and the surrounding scleral tissue need to be obtained.

Fifth, the true orientation of the collagen fiber alignment for the whole sclera is still lacking in literature, and we have attempted to predict it in this study (Fig. 7). Due to the relatively coarse discretization of the regions (eight for the whole posterior shell), we could only report an overall estimate of the preferred collagen fiber orientation within each region, and this might have led to large differences in the preferred fiber orientation between left and right eyes, as observed in Fig. 7. It is currently unknown if inter-eye variations in preferred collagen fiber orientation are large. Even though our estimates of preferred collagen fiber orientation are rough and hampered by the discontinuity between region boundaries, we have more confidence in our tangent moduli and structural stiffness estimates since those quantities were unaffected by a change in regionalization pattern, as obtained from the sensitivity analyses. In 1934, Kokott [39] described spatial mapping of collagen fiber orientation for entire scleral shells using standard histology. However, given the complex lamellar ultrastructure of the sclera, those data were not used in our study as they were crude estimates and did not present the collagen fiber distribution with the reported preferred fiber orientation. Future experimental work will be required to characterize collagen fiber distributions more precisely for entire scleral shells.

Finally, we used eight subregions for the posterior sclera to limit the number of model parameters to be extracted with the inverse FE method to 13. Using more than 13 model parameters dramatically increases the computational time for each simulation [25] and can raise a further concern about the uniqueness of the predicted model parameters. As our primary interest is the biomechanics of the scleral canal and its effects on the contained ONH, we have concentrated four of the eight subregions to model the peripapillary sclera in the vicinity of the ONH. While we tested several other regionalization patterns with fewer regions and/or parameters (data not shown), the combination of eight subregions with 13 parameters produced the best fit with the lowest cost function value (Eq. (2)). It should be noted that the subregional discretization of the posterior sclera resulted in discontinuity of the predicted model parameters (i.e., the preferred fiber orientation and the fiber concentration factor) across the boundaries between the subregions, as shown in Fig. 7.

The experimental and computational methodologies presented here have broad applicability to multi-axial mechanical testing and model parameter prediction of thin soft tissues with varying collagen fiber orientations. We are currently using these methods to characterize the mechanical properties of normal (young and old) and early- and moderate-stage glaucomatous monkey eyes. Mechanical testing and modeling of ocular soft tissues will contribute to our understanding of glaucomatous susceptibility of the ONH [40], posterior scleral damage [10], myopia [30], and a host of other ocular disorders. Since the posterior sclera determines the levels of strain and stress transmitted to the contained ONH and is altered in early experimental glaucoma [10], it is likely to play an important role in glaucomatous damage to the ONH.

Acknowledgment

This work was supported by the NIH (RO1EY11610, Dr. Claude F. Burgoyne). We would like to thank Juan Reynaud for his help with the ION computational server, Jonathan Grimm for his help with the parallel queuing system, Dr. David A. Rice for his help with the ultrasound device and Dr. Richard T. Hart, Dr. Michael D. Roberts, and Dr. Ian A. Sigal for their valuable inputs and shared discussions.

References

- [1] Girard, M. J. A., Downs, J. C., Burgoyne, C. F., and Suh, J.-K. F., 2009, "Peripapillary and Posterior Scleral Mechanics—Part I: Development of an Anisotropic Hyperelastic Constitutive Model," *ASME J. Biomech. Eng.*, **131**, p. 051011.
- [2] Woo, S. L., Kobayashi, A. S., Schlegel, W. A., and Lawrence, C., 1972, "Non-linear Material Properties of Intact Cornea and Sclera," *Exp. Eye Res.*, **14**(1), pp. 29–39.
- [3] Pierscionek, B. K., Asejczyk-Widlicka, M., and Schachar, R. A., 2007, "The Effect of Changing Intraocular Pressure on the Corneal and Scleral Curvatures in the Fresh Porcine Eye," *Br. J. Ophthalmol.*, **91**(6), pp. 801–803.
- [4] Smolek, M., 1988, "Elasticity of the Bovine Sclera Measured With Real-Time Holographic Interferometry," *Am. J. Optom. Physiol. Opt.*, **65**(8), pp. 653–660.
- [5] Greene, P. R., and McMahon, T. A., 1979, "Scleral Creep vs. Temperature and Pressure In Vitro," *Exp. Eye Res.*, **29**(5), pp. 527–537.
- [6] Curtin, B. J., 1969, "Physiopathologic Aspects of Scleral Stress-Strain," *Trans. Am. Ophthalmol. Soc.*, **67**, pp. 417–461.
- [7] Friberg, T. R., and Lacey, J. W., 1988, "A Comparison of the Elastic Properties of Human Choroid and Sclera," *Exp. Eye Res.*, **47**(3), pp. 429–436.
- [8] Siegwart, J. T., Jr., and Norton, T. T., 1999, "Regulation of the Mechanical Properties of Tree Shrew Sclera by the Visual Environment," *Vision Res.*, **39**(2), pp. 387–407.
- [9] Downs, J. C., Suh, J. K., Thomas, K. A., Bellezza, A. J., Burgoyne, C. F., and Hart, R. T., 2003, "Viscoelastic Characterization of Peripapillary Sclera: Material Properties by Quadrant in Rabbit and Monkey Eyes," *ASME J. Biomech. Eng.*, **125**(1), pp. 124–131.
- [10] Downs, J. C., Suh, J. K., Thomas, K. A., Bellezza, A. J., Hart, R. T., and Burgoyne, C. F., 2005, "Viscoelastic Material Properties of the Peripapillary Sclera in Normal and Early-Glaucoma Monkey Eyes," *Invest. Ophthalmol. Visual Sci.*, **46**(2), pp. 540–546.
- [11] Spoerl, E., Boehm, A. G., and Pillunat, L. E., 2005, "The Influence of Various Substances on the Biomechanical Behavior of Lamina Cribrosa and Peripapillary Sclera," *Invest. Ophthalmol. Visual Sci.*, **46**(4), pp. 1286–1290.
- [12] Girard, M., Suh, J. K., Hart, R. T., Burgoyne, C. F., and Downs, J. C., 2007, "Effects of Storage Time on the Mechanical Properties of Rabbit Peripapillary Sclera After Enucleation," *Curr. Eye Res.*, **32**(5), pp. 465–470.
- [13] Phillips, J. R., and McBrien, N. A., 1995, "Form Deprivation Myopia: Elastic Properties of Sclera," *Ophthalmic Physiol. Opt.*, **15**(5), pp. 357–362.
- [14] Wollensak, G., and Spoerl, E., 2004, "Collagen Crosslinking of Human and Porcine Sclera," *J. Cataract Refractive Surg.*, **30**(3), pp. 689–695.
- [15] Schultz, D. S., Lotz, J. C., Lee, S. M., Trinidad, M. L., and Stewart, J. M., 2008, "Structural Factors that Mediate Scleral Stiffness," *Invest. Ophthalmol. Visual Sci.*, **49**, pp. 4232–4236.
- [16] Wei, C., Wang, X., Wang, C., Tao, L., Li, X., and Zhang, Q., 2008, "An Experimental Study on Collagen Content and Biomechanical Properties of Sclera After Posterior Sclera Reinforcement," *Clin. Biomech. (Bristol, Avon)*, **23**, pp. S17–S20.
- [17] Gloster, J., Perkins, E. S., and Pommier, M. L., 1957, "Extensibility of Strips of Sclera and Cornea," *Br. J. Ophthalmol.*, **41**(2), pp. 103–110.
- [18] Quigley, H., and Anderson, D. R., 1976, "The Dynamics and Location of Axonal Transport Blockade by Acute Intraocular Pressure Elevation in Primate Optic Nerve," *Invest. Ophthalmol.*, **15**(8), pp. 606–616.
- [19] Quigley, H. A., and Addicks, E. M., 1980, "Chronic Experimental Glaucoma in Primates. II. Effect of Extended Intraocular Pressure Elevation on Optic Nerve Head and Axonal Transport," *Invest. Ophthalmol. Visual Sci.*, **19**(2), pp. 137–152.
- [20] Erne, O. K., Reid, J. B., Ehmke, L. W., Sommers, M. B., Madey, S. M., and Bottlang, M., 2005, "Depth-Dependent Strain of Patellofemoral Articular Cartilage in Unconfined Compression," *J. Biomech.*, **38**(4), pp. 667–672.
- [21] Kessler, O., Lacatusu, E., Sommers, M. B., Mayr, E., and Bottlang, M., 2006, "Malrotation in Total Knee Arthroplasty: Effect on Tibial Cortex Strain Captured By Laser-Based Strain Acquisition," *Clin. Biomech. (Bristol, Avon)*, **21**(6), pp. 603–609.
- [22] Bellezza, A. J., Rintalan, C. J., Thompson, H. W., Downs, J. C., Hart, R. T., and Burgoyne, C. F., 2003, "Deformation of the Lamina Cribrosa and Anterior Scleral Canal Wall in Early Experimental Glaucoma," *Invest. Ophthalmol. Visual Sci.*, **44**(2), pp. 623–637.
- [23] Downs, J. C., Yang, H., Girkin, C., Sakata, L., Bellezza, A., Thompson, H., and Burgoyne, C. F., 2007, "Three-Dimensional Histomorphometry of the Normal and Early Glaucomatous Monkey Optic Nerve Head: Neural Canal and Subarachnoid Space Architecture," *Invest. Ophthalmol. Visual Sci.*, **48**(7), pp. 3195–3208.
- [24] Bereiter-Hahn, J., 1995, "Probing Biological Cells and Tissues With Acoustic

Microscopy," *Advances in Acoustic Microscopy*, Springer, Berlin.

- [25] Price, K. V., Storn, R. M., and Lampinen, J. A., 2005, *Differential Evolution: A Practical Approach to Global Optimization*, Springer, Berlin.
- [26] Olberding, J. E., and Suh, J.-K. F., 2006, "A Dual Optimization Method for the Material Parameter Identification of a Biphasic Poroviscoelastic Hydrogel: Potential Application to Hypercompliant Soft Tissues," *J. Biomech.*, **39**(13), pp. 2468–2475.
- [27] Sigal, I. A., Flanagan, J. G., Tertinegg, I., and Ethier, C. R., 2008, "Modeling Individual-Specific Human Optic Nerve Head Biomechanics. Part II: Influence of Material Properties," *Biomech. Model. Mechanobiol.*, **8**, pp. 99–109.
- [28] Battaglioli, J. L., and Kamm, R. D., 1984, "Measurements of the Compressive Properties of Scleral Tissue," *Invest. Ophthalmol. Visual Sci.*, **25**(1), pp. 59–65.
- [29] Hernandez, M. R., Luo, X. X., Igoe, F., and Neufeld, A. H., 1987, "Extracellular Matrix of the Human Lamina Cribrosa," *Am. J. Ophthalmol.*, **104**(6), pp. 567–576.
- [30] Rada, J. A., Shelton, S., and Norton, T. T., 2006, "The Sclera and Myopia," *Exp. Eye Res.*, **82**(2), pp. 185–200.
- [31] Komai, Y., and Ushiki, T., 1991, "The Three-Dimensional Organization of Collagen Fibrils in the Human Cornea and Sclera," *Invest. Ophthalmol. Visual Sci.*, **32**(8), pp. 2244–2258.
- [32] Watson, P. G., and Young, R. D., 2004, "Scleral Structure, Organisation and Disease. A Review," *Exp. Eye Res.*, **78**(3), pp. 609–623.
- [33] Girard, M. J. A., Downs, J. C., Burgoyne, C. F., and Suh, J.-K. F., "Experimental Surface Strain Mapping of Porcine Peripapillary Sclera Due to Elevations of Intraocular Pressure," *ASME J. Biomech. Eng.*, **130**(4), p. 041017.
- [34] De Rousseau, C. J., and Bito, L. Z., 1981, "Intraocular Pressure of Rhesus Monkeys (*Macaca Mulatta*). II. Juvenile Ocular Hypertension and Its Apparent Relationship to Ocular Growth," *Exp. Eye Res.*, **32**(4), pp. 407–417.
- [35] Fung, Y. C., 1993, *Biomechanics: Mechanical Properties of Living Tissues*, Springer-Verlag, New York.
- [36] Govindjee, S., and Mihalic, P. A., 1996, "Computational Methods for Inverse Finite Elastostatics," *Comput. Methods Appl. Mech. Eng.*, **136**, pp. 47–57.
- [37] Lu, J., Zhou, X., and Raghavan, M. L., 2007, "Inverse Elastostatic Stress Analysis in Pre-Deformed Biological Structures: Demonstration Using Abdominal Aortic Aneurysms," *J. Biomech.*, **40**(3), pp. 693–696.
- [38] Sigal, I. A., Flanagan, J. G., Tertinegg, I., and Ethier, C. R., 2004, "Finite Element Modeling of Optic Nerve Head Biomechanics," *Invest. Ophthalmol. Visual Sci.*, **45**(12), pp. 4378–4387.
- [39] Kokott, W., 1934, "Das spaltlinienbild der sklera. (Ein beitrage zum funktionellen bau der sklera)," *Klin. Monatsbl. Augenheilkd.*, **92**, pp. 177–185.
- [40] Burgoyne, C. F., Downs, J. C., Bellezza, A. J., Suh, J. K., and Hart, R. T., 2005, "The Optic Nerve Head as a Biomechanical Structure: A New Paradigm for Understanding the Role of IOP-Related Stress and Strain in the Pathophysiology of Glaucomatous Optic Nerve Head Damage," *Prog. Retin. Eye Res.*, **24**(1), pp. 39–73.